42st European Rotorcraft Forum

104

CFD ASSESSMENT OF THE HELICOPTER AND GROUND OBSTACLES AERODYNAMIC INTERFERENCE

G. Gibertini*, G. Droandi*, D. Zagaglia*, P. Antoniazza*, A. Oregio Catelan*

*Dipartimento di Scienze e Tecnologie Aerospaziali – Politecnico di Milano
Campus Bovisa, Via La Masa 34, 20156 Milano, Italy
e-mail: giuseppe.gibertini@polimi.it

Keywords: Helicopter, Aerodynamics, Rotor, Vortex-Interaction, Computational Fluid Dynamics, Ground Obstacle.

Abstract

The helicopter is a very versatile flying machine that is often required to operate in confined areas or close to vertical obstacles such as buildings, ships and mountain walls. Therefore, the aerodynamic interaction between a helicopter and the surrounding obstacles has recently become a promising research topic in the rotorcraft field. In the present paper, the behaviour of a helicopter operating in the proximity of a ground obstacle is investigated using numerical simulations. Calculations were performed on the geometry used at Politecnico di Milano to carry out a systematic experimental study of the helicopter/obstacles aerodynamic interference. High-accuracy steady calculations were carried out using a compressible Navier-Stokes solver developed in-house. In this framework, an actuator disk model is used to reproduce the rotor effects. Blade loads prescribed on the actuator disk were computed using a low-accuracy aerodynamic solver based on the strip theory. The solvers were coupled through a weak coupling algorithm that allowed to find more realistic load maps in the rotor disk modifying the initial inflow prescribed by the strip theory using induced velocities provided by the Navier-Stokes solver. Numerical results were validated using experimental data and enabled to achieve a detailed insight about the aerodynamic interaction occurring when a helicopter is operating near a ground obstacle.

NOMENCLATURE

C_p	=	Pressure coefficient
C_Q	=	Rotor torque coefficient, $Q/(\rho\pi\Omega^2R^5)$
C_T	=	Rotor thrust coefficient, $T/(\rho\pi\Omega^2R^4)$
p	=	Local pressure
p_∞	=	Reference pressure
Q	=	Rotor torque
Ω	=	Angular speed
R	=	Rotor radius
ρ	=	Air density
T	=	Rotor thrust
v_{ind}	=	Induced velocity

1 INTRODUCTION

The helicopter is a very versatile flying machine which is often required to operate within confined areas, due to its capability of managing hovering flight. The aerodynamic interaction between the rotor-induced wake and the surrounding obstacles, such as buildings and mountain walls, typically generates a degradation of the helicopter performance and high compensatory workload for the pilot.

Several degrees of approximation can be employed for the fully-coupled aerodynamic simulation of the helicopter-obstacle interaction. The most natural and possibly high-fidelity method is to actually solve the flow around each rotating blade. This method allows to capture the time-dependent features of the rotor wake and the aerodynamic interference between the rotor and the obstacle, but it is extremely onerous from a time and computer-memory point of view, thus often making these kind of simulations unaffordable.

A further step of approximation can be achieved by modelling the effect of the rotor on the flow rather than solving the flow around the blades, using the Actuator Disk (AD) method in order to make the numerical simulation less computationally onerous. This method consists in adding source terms, which are dependent on the local blade loading, in the flow momentum and energy equations in order to enforce a pressure jump across the rotor disc. The standard AD model prescribes a revolution-averaged disk loading, at the cost of losing the time-dependent description of the blade passing. Once again a further degree of approximation can be introduced, by choosing a closed-loop or open-loop description of the AD. In the open-loop approach the pressure jump on the rotor is imposed *a priori* based on the local disk loading as in [1, 2, 3], whereas the closed-loop approach updates the rotor inflow according to the computed flow-field, at the cost of a few steady-state iterations, as implemented in [4] by Rajagopalan et al. The inherent time-dependency of the wake structures can be recovered using an Unsteady Actuator Disk (UAD) or Actuator Blade Model [5, 6], where the momentum source on the disk follow each blade rather than being averaged over a complete revolution.

This paper presents the numerical assessment of the helicopter-obstacle aerodynamic interaction in hovering flight, in absence of external wind. Numerical calculations were carried out with the Computational Fluid Dynamic (CFD) code ROSITA (ROtorcraft Software ITAly) developed at Politecnico of Milano [7] and based on the solution of the compressible Reynolds Averaged Navier-Stokes (RANS) equations coupled with the one-equation turbulence model of Spalart-Allmaras. A steady AD model already embedded in ROSITA and reproducing the effects of the rotor blades using a disk having the same diameter of the rotor itself [8] was employed for the calculations. Blade loads prescribed on the AD were computed using the code HERA (HElicopter Rotor Analysis) recently developed at Politecnico di Milano and based on the simple strip theory and two-dimensional airfoil section aerodynamic characteristics. The HERA solver was coupled with the CFD code ROSITA using a closed-loop coupling strategy. The CFD simulations were validated through comparison with an experimental database [9] produced at Politecnico Milano in the framework of the The GARTEUR Action Group 22 "Forces on Obstacles in Rotor Wake" [10] comprising several universities (Politecnico di Milano, University of Glasgow, National Technical University of Athens) and research institutes (CIRA, DLR, ONERA, NLR). This database comprised load measurements on the rotor, pressure measurement on the obstacle and time-averaged Particle Image Velocimetry (PIV) measurements of the flow-field.

2 EXPERIMENTAL SETUP

In the present work, the case of a hovering helicopter flying in the proximity of a ground obstacle is investigated using CFD simulations. Numerical calculations were performed on the geometry described by Gibertini et al. [9] and the experimental database gathered at Politecnico di Milano was used to assess the effectiveness of numerical simulations. The database comprises a series of

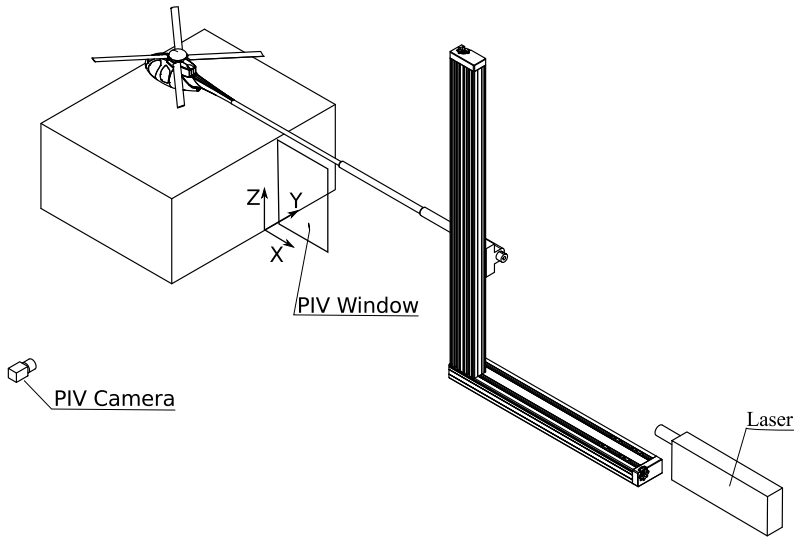

Figure 1: Schematic of the Test Rig and experimental setup.

tests reproducing hovering flight conditions for different helicopter positions with respect to a simplified volume with a parallelepiped shape. The test rig sketched in Figure 1 essentially consisted of a helicopter model, inspired by the MD-500, and an obstacle which represented an ideal building. For each test condition analysed during the experiments force measurements on the helicopter rotor and pressure measurements on the obstacle surfaces have been acquired. Furthermore, the PIV technique was employed to survey the flow field between the helicopter and the obstacle in the most relevant conditions. The adopted reference system is represented in Figure 1 too. The origin of the reference system was located on the floor, at the mid-span of the front face.

The helicopter model was held by a horizontal strut fixed to a system of two motorised orthogonal sliding guides in order to allow the helicopter displacement with respect to the obstacle. The rotor had four untwisted and untapered rectangular blades with a chord of $c = 0.032$ m and radius of $R = 0.375$ m. The adopted airfoil was a NACA 0012. No swash plate was present, so the collective blade pitch angle was fixed to 10°. A rotational speed Ω of 2480 RPM was maintained during all the tests. The resulting Mach number and Reynolds number at the blade tip were $M_{Tip} = 0.286$ and $Re_{Tip} = 2.12 \times 10^6$, respectively. The forces and moments acting on the rotor were measured by means of a six-component balance nested inside the fuselage. A Hall effect sensor produced one-per-revolution signal in order to monitor the rotational frequency.

The obstacle model was a aluminium alloy parallelepiped, whose dimensions were 0.45 m ×0.8 m ×1.0 m. The building model was equipped with 150 pressure taps, of which 31 lay on the top plate, 21 lay on the side plate and 48 lay on the front plate. The remaining taps were located on the other three faces, which were not considered. The pressures were acquired by means of four low-range 32-port scanners embedded inside the building model.

The PIV system comprised a Litron NANO-L-200-15 Nd:Yag double-pulse laser with an output energy of 200 mJ and wavelength of 532 nm, and an Imperx ICL-B1921M CCD camera with a 12-bit, 1952×1112 pixel array. The laser was positioned on the floor so that the laser sheet was aligned with the symmetry plane of both the obstacle and the helicopter models. As shown in Figure 1, the PIV measurement window was 300 mm ×400 mm and it was placed in the symmetry plane of the problem ($Y/R = 0$). In order to achieve better resolution of the image pairs, the measurement area comprised two adjacent windows, one on top of the other, with a small overlapping band between them. A PIVpart30 particle generator by PIVTEC with Laskin atomizer nozzles was used for the seeding. The image-pairs analysis were carried out by means of the PIVviev 2C software.

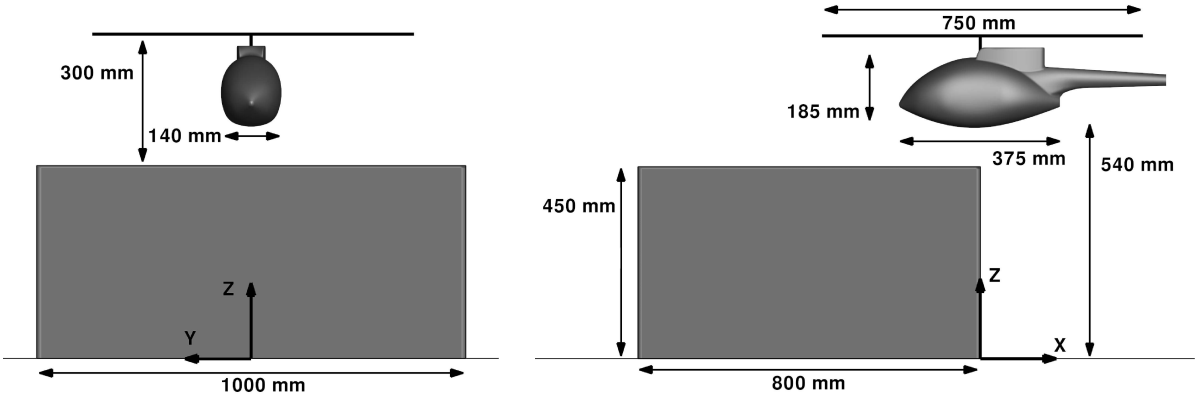

(a) Frontal view

(b) Lateral view

Figure 2: Scheme of the helicopter/obstacle set up and reference system.

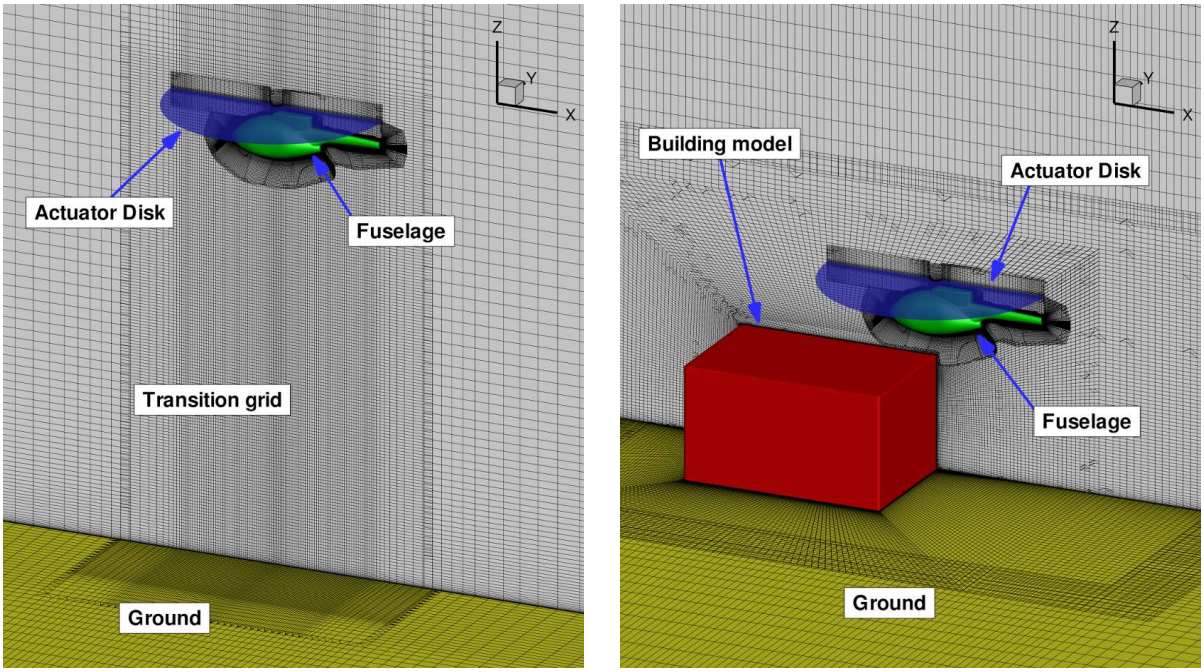

(a) Grid for ground effect evaluation

(b) Grid for helicopter/building interference evaluation

Figure 3: Sketch of computational grids for a) ground effect evaluation without the building model, and for b) helicopter/building model aerodynamic interference evaluation.

3 NUMERICAL SETUP

Numerical calculations were carried out using the high-accuracy CFD code ROSITA coupled with the low-accuracy HERA solver based on the strip theory. In this framework, a steady-state approach was employed and an AD model was used to represent the rotor effects instead of simulating the flow around rotating blades. The use of the steady-state assumption together with the AD model give a strong reduction of both grid complexity and computational times required with respect to the unsteady approach. Blade loads prescribed on the AD were computed using the aerodynamic solver HERA that allowed to easily predict the rotor performance.

3.1 Flow solver ROSITA

The CFD code ROSITA numerically integrates the compressible Reynolds Averaged Navier-Stokes (RANS) equations, coupled with the one-equation turbulence model by [11]. Multiple moving multiblock grids can be employed to build an overset grid system using the Chimera technique. To allow the solution of the flow field in overset grid systems, the Navier-Stokes equations are formulated in terms of the absolute velocity, expressed in a relative frame of reference linked to each component grid. The equations are discretised in space by means of a cell-centered finite-volume implementation of the Roe's scheme [12]. Second order accuracy is obtained through the use of Monotonic Upstream-Centered Scheme for Conservation Laws (MUSCL) extrapolation supplemented with a modified version of the Van Albada limiter, as suggested by Venkatakrishnan [13]. The Gauss theorem and a cell-centered discretization scheme are used to compute the viscous terms of the equations. Time advancement is carried out with a dual-time formulation [14], employing a 2^{nd} order backward differentiation formula to approximate the time derivative and a fully unfactored implicit scheme in pseudo-time. The equation for the state vector in pseudo-time is non-linear and is solved by sub-iterations accounting for a stability condition, as shown by Hirsch [15] for viscous flow calculations. The generalized conjugate gradient (GCG) is employed to solve the resulting linear system. A block incomplete lower-upper preconditioner is used in this context.

The connectivity between the different grids that represent the whole flow field is computed using the Chimera technique. The approach adopted in ROSITA is derived from the one originally proposed by Chesshire and Henshaw [16], with some modifications to further improve robustness and performance of the algorithm. During the tagging procedure, the domain boundaries with solid wall conditions are firstly identified and all points in overlapping grids that fall close to these boundaries are marked as holes (seed points). Then, an iterative algorithm identifies the donor and fringe points and lets the hole points grow from the seeds until they entirely fill the regions outside the computational domain. Oct-tree and alternating digital tree (ADT) data structures are employed in order to speed up the search of donor points.

When two or more overlapping surface grids are present in the nested grid system, the so-called "zipper-grid" technique proposed by Chan and Buning [17] is used. This technique consists in eliminating the overlapped surface cells using triangles to fill the gap. The integration of the aerodynamic loads is performed on the resulting hybrid mesh.

The ROSITA solver is fully capable of running in parallel on large computing clusters. The parallel algorithm is based on the message passing programming paradigm and the parallelization strategy consists in distributing the grid blocks among the available processors. Each grid block can be automatically subdivided into smaller blocks by the solver to obtain an optimal load balancing.

3.2 Rotor solver HERA

The helicopter rotor performance solver HERA allows to evaluate the performance of a given rotor flying in a certain condition. The code is based on the classical blade element theory [18] that is usually employed for the analysis of helicopter rotors. As well known, the blade element approach offers a simple, but sufficient accurate, method to estimate the airloads on rotor blades [19]. In particular, it allows to find the time-averaged ariloads at various points of the rotor disk once the time-averaged induced velocity maps were known on the rotor disk.

The equations implemented in the HERA code are formally generalized to large angles. The airfoil data necessary to the solver are previously stored in tables for a wide range of angles of attack, Reynolds and Mach numbers (two-dimensional CFD results).

3.3 Coupling strategies

The CFD code ROSITA and the HERA solver were coupled through a weak coupling algorithm. An AD model embedded in ROSITA was used to reproduce the effects of the rotor blades in the flow-filed. Blade axial, tangential and radial aerodynamic force components were prescribed on the AD, a disk having the same diameter of the rotor itself, and were computed using the HERA solver that required the induced axial, tangential and radial velocity maps as an input. The rotor inflow is updated at each iteration depending on the computed CFD flow-field. This procedure was repeated until the rotor thrust variation resulted lower than a prescribed tolerance. The convergence was usually reached within 5-10 cycles. This approach allowed to find more realistic load maps on the rotor disk modifying the initial inflow prescribed by the HERA solver using the induced velocity maps provided by ROSITA. This method is

computationally efficient and allowed an accurate prediction of the average flow-field and of the rotor performance. With the aim of increasing the computational stability of the coupling strategy, a relaxation parameter was introduced in the calculation of the updated inflow maps by considering a linear combination of the velocity components at the last two cycles.

3.4 Numerical model

Steady coupled simulations were performed to study the behaviour of a helicopter both in the proximity of a building model or on a free surface. The Cartesian reference system adopted for the calculation is shown in Figure 2. The final computational grids were composed by 4 structured multi-block meshes, for a total number of about 8×10^6 elements. In particular, a squared background mesh reproducing the flow region above the ground was discretised with a H topology and was composed by a total number of 1.8×10^6 elements. The outer boundaries were located 42 R from the grid centre and parallel to the ground and 13 R above the ground. An O-H grid multiblock meshing topology was used to limit the global grid size and to ensure a very good nodes distribution and orthogonality in the proximity of the building model surface. On the other hand, an O grid topology was used to discretise the flow region around the fuselage. Both the building model and fuselage grids were composed by a total number of 3×10^6 elements. For all those cases in which the obstacle was not considered, the building model grid was replaced by a flow transition grid having the same total number of elements. Finally, a cylindrical grid of about 0.3×10^6 elements was used to represent the AD. A no-slip boundary condition was applied on the ground, on the building and on the fuselage while farfiled conditions were imposed on the other sides of the background mesh. The nested grid systems employed for calculations are reported in Figure 3.

4 RESULTS

4.1 Ground effect simulations

CFD simulations of the helicopter in ground effect, without the obstacle, were carried out as a preliminary validation test. The helicopter was placed at different heights with respect to the ground, in particular $Z/R = 1$, 1.6, 2.5, 5. The condition at $Z/R = 5$, where the effects of the ground are negligible, was chosen as the reference condition with respect to which all the load data are represented in the following sections. This particular condition will be referred as Out of Ground Effect (OGE) condition from now on.

An example of rotor load convergence history (helicopter placed at $Z/R = 5$ above the ground, without the building) is reported in Figure 4(a) and 4(b) where the thrust coefficient C_T and the torque coefficient C_Q of the rotor are shown as function of the ROSITA/HERA coupling cycles. In these pictures, numerical coefficients are also compared with the corresponding values measured in the experiment showing a good agreement between them.

Table 1 presents the comparison between the measured and computed thrust coefficient, torque coefficient and figure of merit for the OGE condition ($Z/R = 5$). The thrust coefficient is very well captured (the discrepancy with respect to the experimental value is less than 1 %), while the torque prediction and consequently the Figure of Merit prediction is less accurate, but nevertheless acceptable. This might be due to the relative low Tip Reynolds number of the experiment (and therefore of the simulation, approximately $2 \cdot 10^5$), which could prevent a very accurate prediction of the viscous contribution to the rotor torque.

	$C_{T,OGE}$	$C_{Q,OGE}$	FM_{OGE}
Exp.	$7.05 \cdot 10^{-3}$	$7.50 \cdot 10^{-3}$	0.557
CFD	$7.10 \cdot 10^{-3}$	$8.17 \cdot 10^{-3}$	0.518
Error	0.7 %	8.9 %	7 %

Table 1: Thrust, torque coefficients and figure or merit at $Z/R = 5$ (OGE). Comparison between experimental [9] and numerical results.

The comparison between the measured and computed thrust and torque coefficient for the ground effect test is presented in Figure 5. As previously stated, both the experimental and numerical results will be presented from now on divided by their respective OGE values, in order to appreciate their variation from the reference condition. As it can be appreciated from Figure 5(a), the ground effect is captured fairly well, as a gradual thrust increase when the helicopter is closer to the ground. In particular, a 9 % increase prediction with respect to the OGE value can be observed, versus the measured 13 %. The torque variation is quite limited with respect to the thrust one (less than 3 %), but the agreement between numerical and experimental results is nevertheless good.

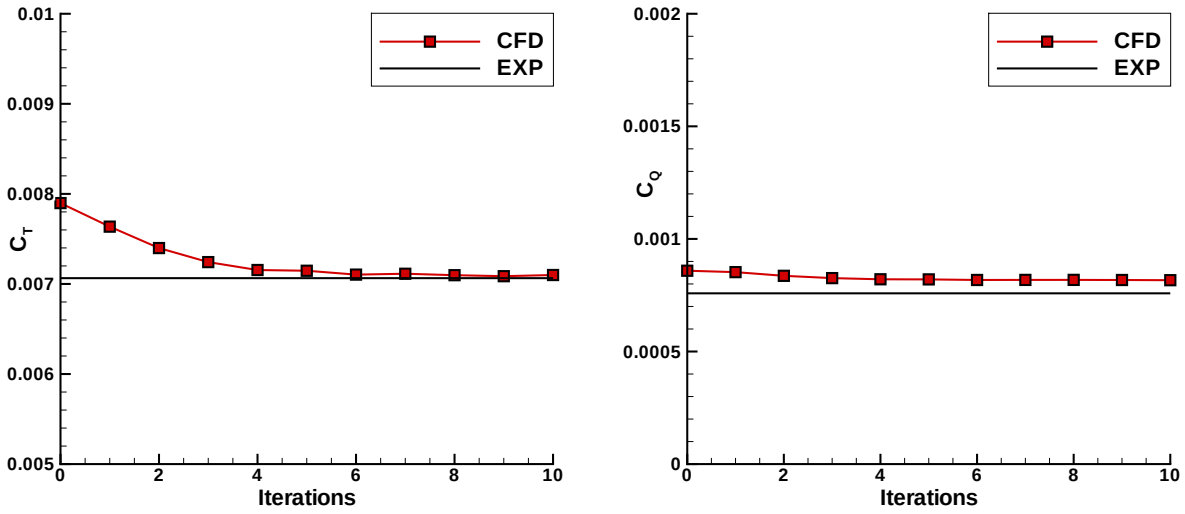

(a) Thrust coefficient C_T

(b) Torque coefficient C_Q

Figure 4: Thrust and torque coefficient evolution over the iteration cycles: comparison between measured [9] and computed values.

The physics behind the ground effect seems to be well captured by the numerical method, and this is testified also by Figure 6, where the azimuth-averaged induced velocity is presented. A gradual reduction of the vertical induced velocity can be observed as the helicopter is placed closer to the ground, causing an increased blade angle of attack and consequently an increased thrust, as prescribed by the ground effect.

4.2 Helicopter-Obstacle interaction

The results of the CFD simulations for the helicopter-obstacle interaction are presented in this section. In particular, the helicopter was placed in different positions at $Z/R = 2$ along the X-direction with respect to the obstacle in the symmetry plane of the problem ($Y/R = 0$) in order to simulate a slow horizontal approach to the obstacle upper surface, which corresponds to Test 5 of Ref. [9]. Figure 7 presents the position of the rotor centre for the different test condition of the numerical and experimental investigations respectively. The analysed configurations span from $X/R = -1.07$ (TN1), where the helicopter is placed above the centre of the obstacle upper-surface, to $X/R = 1$ (TN6), where the helicopter is no longer over the obstacle. The complete list of test points and available measurements is reported in table 2.

4.2.1 Airloads results

The comparison between the computed and measured rotor loads for all the considered test number are presented in Figure 8. Both the thrust (Figure 8(a)) and torque (Figure 8(b)) coefficients were divided by their respective OGE values as in the previous section.

As it can appreciated from figure Figure 8(a), the rotor undergoes a gradual ground effect reduction as it is moved from the top of the obstacle , $X/R = -1.07$, to the outermost position $X/R = 1$. This trend is also well represented by the results of the numerical simulations, even though a slight discrepancy can be noticed, which was nevertheless present also in the IGE test of Figure 5(a). The variation of the thrust coefficient is well explained also by Figure 9, where a gradual induced velocity reduction can be appreciated for decreasing X/R, i.e. when the helicopter is placed over the obstacle. Torque variations appear to be well predicted by the numerical simulations (Figure 8(b)), as in the IGE test.

4.2.2 Flow field analysis

Figure 10 presents the comparison between the computed flow fields and those obtained by means of PIV. The PIV measurements were carried out in the measurement window of Figure 1 placed in the symmetry plane of the problem, for test number 2, 4 and 6, corresponding to $X/R = -1$, 0 and 1. The

TN	X/R	Y/R	Z/R	CFD	Load Meas.	Pressure Meas.	PIV
TN1	-1.07	0	2	×	×		
TN2	-1	0	2	×	×	×	×
TN3	-0.5	0	2	×	×		
TN4	0	0	2	×	×	×	×
TN5	0.5	0	2	×	×		
TN6	1	0	2	×	×	×	×

Table 2: Numerical test matrix and list of the available measurements for each test point.

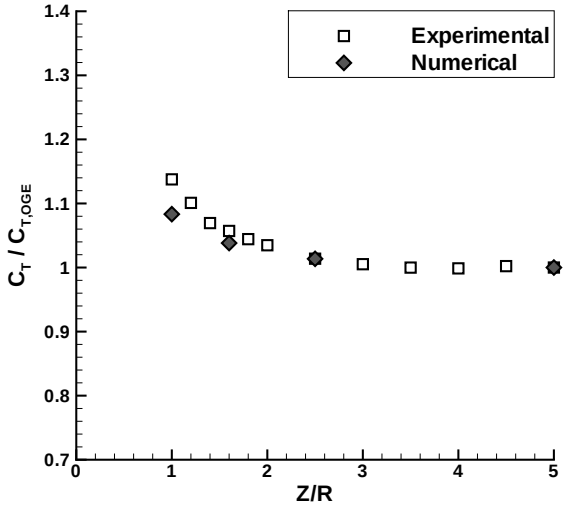

(a) Thrust coefficient C_T

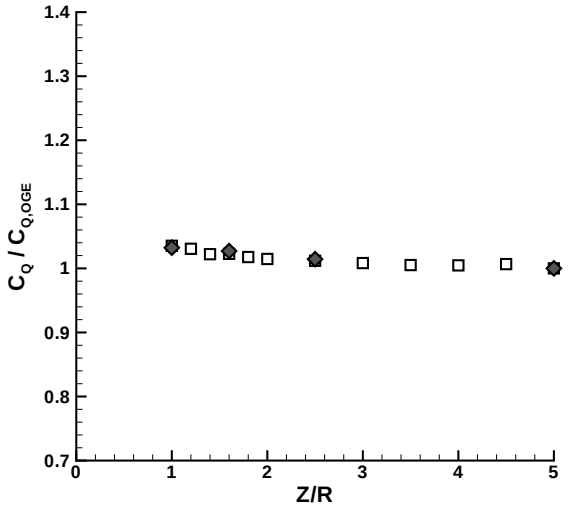

(b) Torque coefficient C_Q

Figure 5: Rotor performance as function of rotor distance from the floor Z/R. Comparison between numerical and experimental results [9].

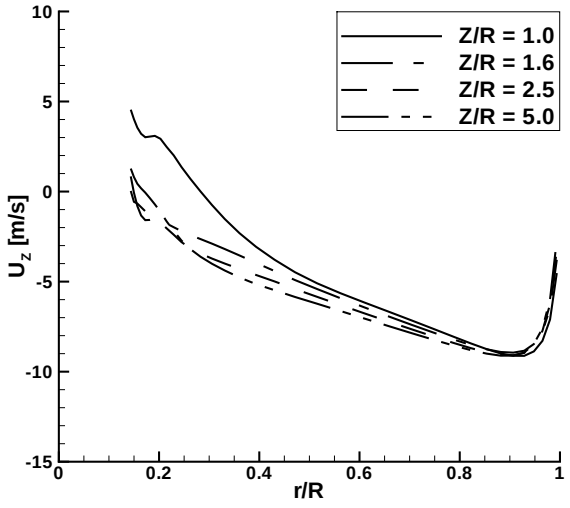

Figure 6: Vertical induced velocity as function of non-dimensional radial position.

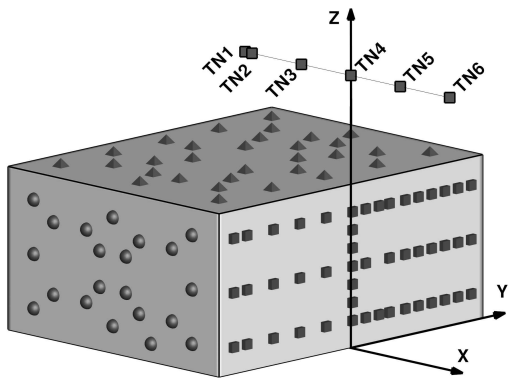

Figure 7: Schematic of the experimental and numerical investigation points and location of the pressure taps on the obstacle. Each investigation point represents the position of the rotor centre in that particular configuration.

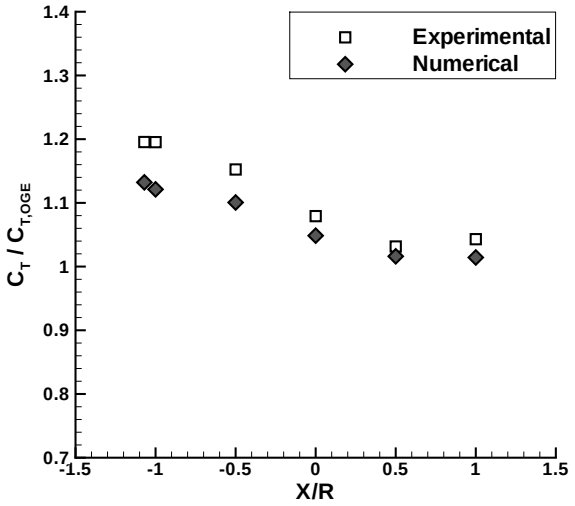

(a) Thrust coefficient C_T

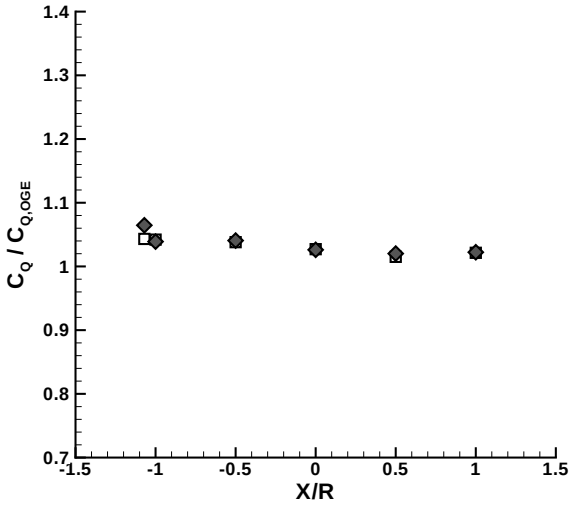

(b) Thrust coefficient C_Q

Figure 8: Rotor performance as function of rotor horizontal position with respect to the obstacle X/R, at $Z/R = 2$. Comparison between numerical and experimental results [9].

measured and computed flow fields are presented in Figure 10 by means of the in-plane velocity magnitude contours and in-plane streamlines patterns. In general a fairly good agreement can be noticed between the CFD and PIV flow-fields. The main flow structures and their features appear to be well captured by the CFD analysis, thus validating the adopted numerical approach for this kind of aerodynamic interactions.

Figure 10(a) and 10(b) clearly show a high-speed layer issued from the obstacle upper surface, when

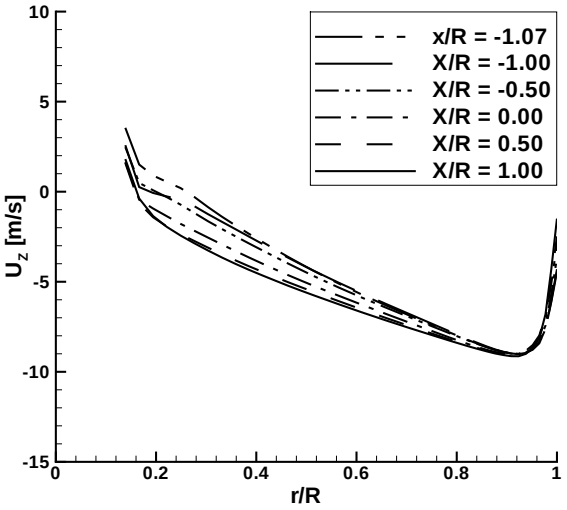

Figure 9: Azimuth-averaged induced velocity for different rotor positions with respect to the building edge.

the helicopterip is positioned at $X/R = -1$. This layer originates from the rotor rear-wake deflected by the obstacle, which induces a large clockwise recirculating region ahead of the front face due to the separation at the obstacle edge. For the test condition at $X/R = 0$ of Figure 10(c) and 10(d), just half of the rotor wake impinges on the building model roof. A larger part of the rotor wake starts to be deflected in this region which is evident from the high-speed layer on the top-left part of the measurement window, which then merges with the rear rotor wake. The clockwise recirculation region produced by the air blowing from the roof is still present, but it is closer to the obstacle with respect to the previous case. Eventually, for $X/R = 1$, the rotor wake no longer impinges on the obstacle upper surface. The front slipstream skims the obstacle front surface and induces a large counterclockwise recirculation region that can be well appreciated both in the experimental (Figure 10(f)) and numerical results (Figure 10(e)).

These substantial changes in the flow topology obviously imply very different pressure patterns on the obstacle. Figure 11 presents the comparison between the computed and measured pressure coefficients on the three considered obstacle faces. Due to the lacking of a free-stream velocity, the pressure coefficients were computed using the following formula:

$$C_p = \frac{p - p_\infty}{\frac{1}{2}\rho v_{ind}^2}, \quad (1)$$

where v_{ind} is the rotor induced velocity, that can be estimated using the momentum theory as:

$$v_{ind} = \Omega R \sqrt{\frac{C_{T,OGE}}{2}}. \quad (2)$$

An overall good agreement can be found for all the configurations. Starting from $X/R = -1$, an high pressure region corresponding to the impingement area of the rotor wake can be appreciated in Figure 11(a) and 11(b). The front face of the obstacle presents a slight depression. When the rotor centre lies exactly on the building edge ($X/R = 0$, Figure 11(c) and 11(d)), the pressure distributions on the different faces of the building indicate the presence of a complex flow structure that was markedly non-symmetrical. The diagonal pattern on the front face is probably related to the helicoidal structure of the rotor wake, which is nevertheless well captured by the numerical simulations. For $X/R = 1$ (Figure 11(e) and 11(f)), the helicopter wake no longer affects the upper surface of the obstacle. However an over-pressure region can be appreciated on the front face due to the rotor wake that, after being deflected by the ground, impinges on the lower part of the obstacle.

5 CONCLUSIONS

The numerical assessment of the helicopter-obstacle aerodynamic interaction in hovering flight, in absence of external wind, has been presented in the present paper. Numerical calculations have been carried out by coupling the CFD code ROSITA with the helicopter rotor aerodynamic performance solver HERA. An actuator disk was employed to represent the rotor in the flow-field and a steady-state approach has been used to carry out the CFD simulations. ROSITA and HERA has been coupled through a weak coupling strategy where the rotor inflow is updated at each iteration depending on the computed CFD flow-field. Such a method was computationally efficient and allowed for accurately predicting both the average flow-field and the rotor performance.

The CFD simulations have been validated through comparison with an experimental database previously produced at Politecnico Milano, comprising load measurements on the rotor, pressure measurement on the obstacle and time-averaged PIV measurements of the flow-field.

In general the loads acting on the rotor, the flow structures resulting in this interaction and the pressure patterns on the obstacle were predicted fairly well, thus validating the adopted numerical approach for this kind of aerodynamic interactions.

Copyright Statement

References

[1] Crozon, C., Steijl, R., and Barakos, G., "Numerical Study of Helicopter Rotors in a Ship Airwake," *Journal of Aircraft*, Vol. 51, No. 6, 2014, pp. 1813–1832.

[2] Polsky, S. and Wilkinson, C., "A computational study of outwash for a helicopter operating near a vertical face with comparison to experimental data," *AIAA–2009–5684*, AIAA Modeling and Simulation Technologies Conference, Chicago, IL, USA, August 10–13 2009.

[3] Wakefield, N., Newman, S., and Wilson, P., "Helicopter flight around a ship's' superstructure," *Proceedings of the Institution of Mechanical Engineers, Part G: Journal of Aerospace Engineering*, Vol. 216, No. 1, 2002, pp. 13–28.

[4] Rajagopalan, G., Niazi, S., Wadcock, A., G.K.Yamauchi, and Silva, M., "Experimental and Computational Study of the Interaction between a Tandem-Rotor Helicopter and a ship," *American Helicopter Society* 61^{th} *Annual Forum*, June 1-3 2005.

[5] Lynch, C., Prosser, D., and Smith, M., "An efficient actuating blade model for unsteady rotating system wake simulations," *Computers & Fluids*, Vol. 92, 2014, pp. 138–150.

[6] Valentini, M., Droandi, G., Masarati, P., and Quaranta, G., "Unsteady Actuating Blade Model for CFD/CSD Analysis of a Tiltrotor," *41st European rotorcraft forum*, September 1-4 2015.

[7] Biava, M., *RANS computations of rotor/fuselage unsteady interactional aerodynamics*, Ph.D. thesis, Politecnico di Milano, Milano, Italy, 2007.

[8] Biava, M., Valentini, M., and Vigevano, L., "Trimmed Actuator Disk Modeling for Helicopter Rotor," 39^{th} European Rotorcraft Forum, Moscow, Russia, September 3–6 2013.

[9] Gibertini, G., Grassi, D., Parolini, C., Zagaglia, D., and Zanotti, A., "Experimental investigation on the aerodynamic interaction between a helicopter and ground obstacles," *Proceedings of the Institution of Mechanical Engineers, Part G: Journal of Aerospace Engineering*, Vol. 229, No. 8, 2015, pp. 1395–1406.

[10] Pahlke, K., "GARTEUR helicopter cooperative research," *36th European rotorcraft forum*, September 7-9 2010.

[11] Spalart, P. and Allmaras, S., "One equation model for aerodynamic flows," *AIAA 92-0439*, 30^{th} AIAA Aerospace Science Meeting & Exhibit, Reno, Nevada, USA, January 6–9, 1992.

[12] Roe, P. L., "Approximate Riemann Solvers, Parameter Vectors and Difference Schemes," *Journal of Computational Physics*, Vol. 43, 1981, pp. 357–372.

[13] Venkatakrishnan, V., "On the accuracy of limiters and convergence to steady state solutions," *AIAA 1993–880*, 31^{st} AIAA Aerospace Science Meeting & Exhibit, Reno, Nevada, USA, 1993.

[14] Jameson, A., "Time Dependent Calculations Using Multigrid with Applications to Unsteady Flows past Airfoils and Wings," *AIAA 91–1596*, 10^{th} AIAA Computational Fluid Dynamics Conference, Honolulu, HI., 1991.

[15] Hirsch, C., *Numerical computation of internal and external flows*, John Wiley & Sons, 1988.

[16] Chesshire, G. and Henshaw, W. D., "Composite overlapping meshes for the solution of partial differential equations," *Journal of Computational Physics*, Vol. 90, 1990, pp. 1–64.

[17] Chan, W. and Buning, P., "Zipper grids for force and moment computation on overset grids," *AIAA 1995–1681*, 12^{th} AIAA Computational Fluid Dynamics Conference, San Diego, CA, USA, 1995.

[18] Johnson, W., *Helicopter Theory*, Princeton University Press, Princeton, New Jersey, USA, 1980.

[19] Gur, O. and Rosen, A., "Comparison between Blade-Element Models," *The Aeronautical Journal*, Vol. 112, No. 1138, December 2008, pp. 689–704.

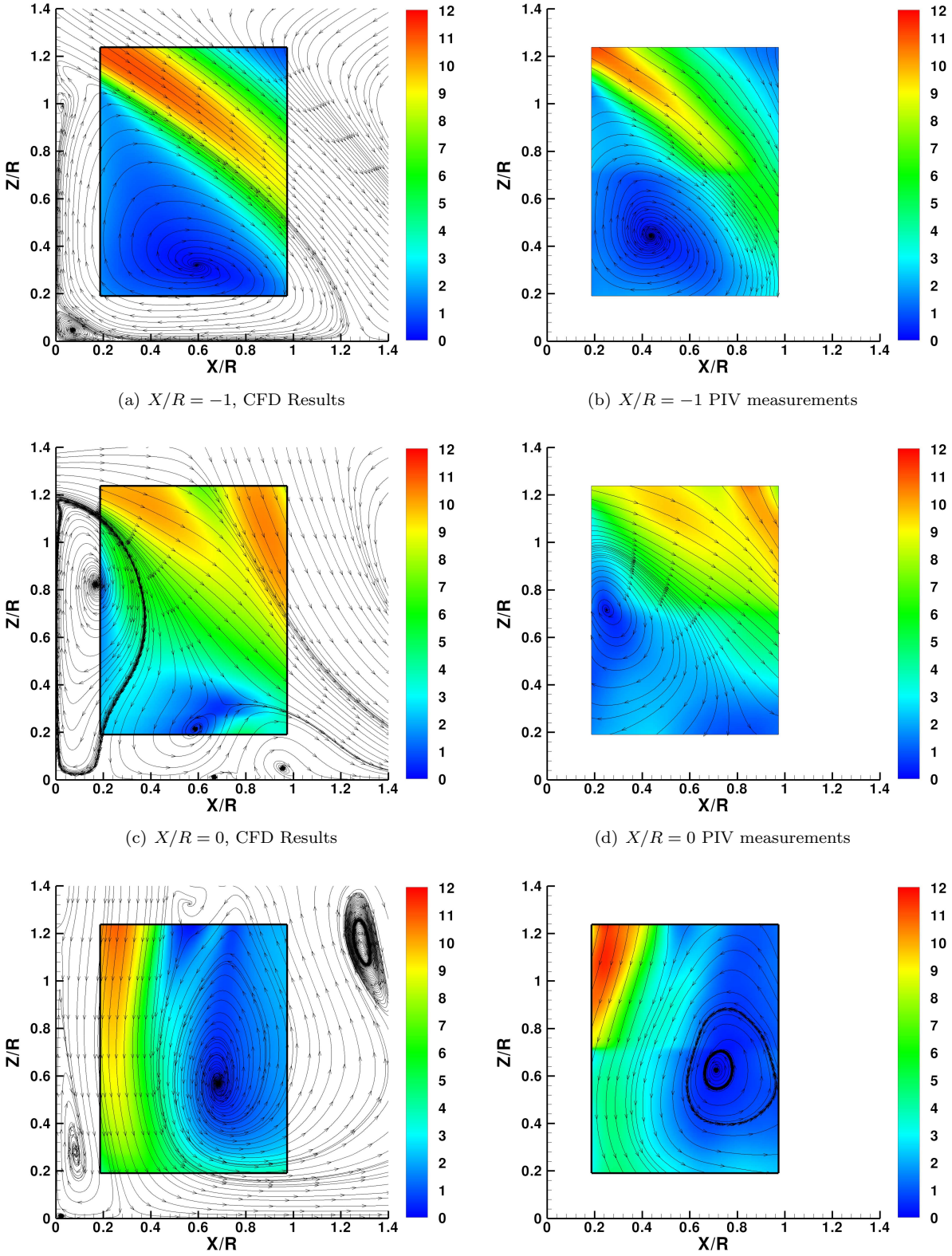

(a) $X/R = -1$, CFD Results

(b) $X/R = -1$ PIV measurements

(c) $X/R = 0$, CFD Results

(d) $X/R = 0$ PIV measurements

(e) $X/R = 1$, CFD Results

(f) $X/R = 1$ PIV measurements

Figure 10: In-plane velocity contours (m/s) and streamlines for different rotor positions with respect to the obstacle edge. Comparison between the numerical simulations and the measured PIV velocity fields [9].

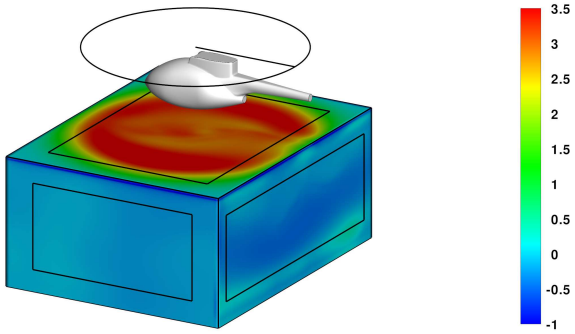

(a) $X/R = -1$, CFD Results

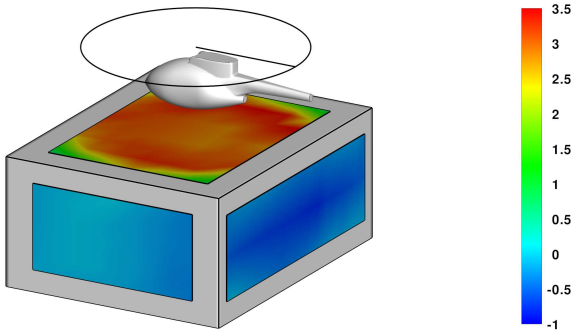

(b) $X/R = -1$ Experimental results

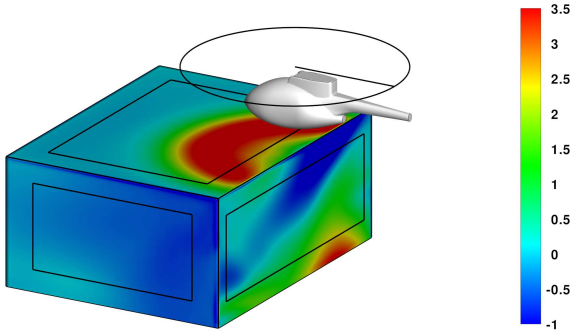

(c) $X/R = 0$, CFD Results

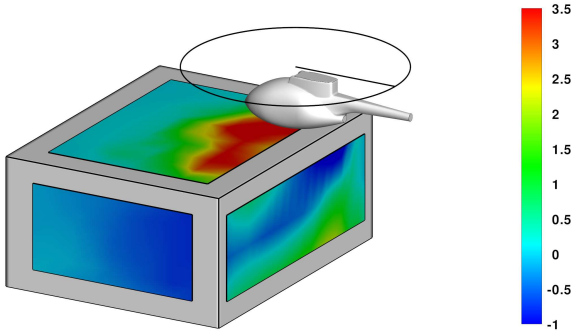

(d) $X/R = 0$ Experimental results

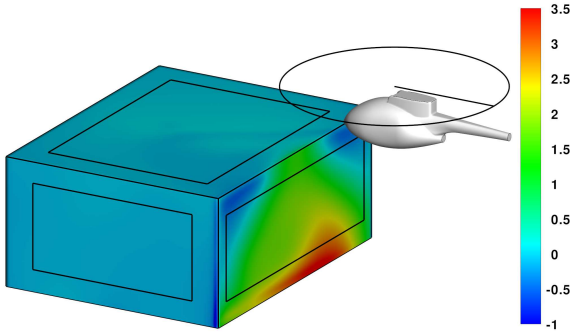

(e) $X/R = 1$, CFD Results

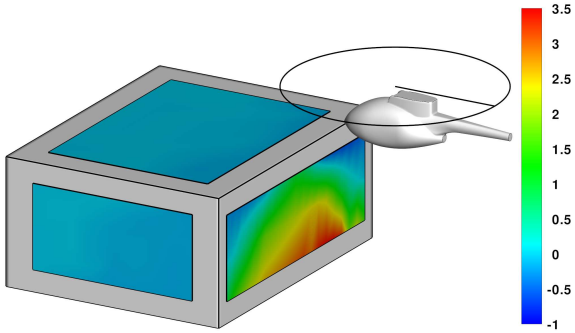

(f) $X/R = 1$ Experimental results

Figure 11: Pressure coefficient contours on the obstacle for different rotor positions with respect to the obstacle edge. Comparison between the numerical simulations and the measured pressures [9].